IEEE Access
Multidisciplinary | Rapid Review | Open Access Journal

Received March 21, 2020, accepted March 27, 2020, date of publication March 30, 2020, date of current version April 14, 2020.

Digital Object Identifier 10.1109/ACCESS.2020.2984281

Pole Optimization and Thrust Ripple Suppression of New Halbach Consequent-Pole PMLSM for Ropeless Elevator Propulsion

XIAOZHUO XU[1], (Member, IEEE), ZHEN SUN[1], BAOYU DU[2], AND LIWANG AI[1], (Member, IEEE)

[1]School of Electrical Engineering and Automation, Henan Polytechnic University, Jiaozuo 454000, China
[2]School of Mechanical and Power Engineering, Henan Polytechnic University, Jiaozuo 454000, China

Corresponding author: Zhen Sun (sunzhen@home.hpu.edu.cn)

This work was supported in part by the National Natural Science Foundation of China under Grant U1504506, in part by the Key Research of Development and Promotion of Henan Province under Grant 192102210073, and in part by the Foundation for University Key Teachers from Henan Province of China under Grant 2017GGJS051.

ABSTRACT Permanent magnet linear synchronous motors (PMLSM) has the advantages of high speed, high thrust density, high power density, high power factor and high reliability. In order to save permanent magnet (PM) materials and reduce magnetic leakage, a new type of PMLSM with Halbach consequent-pole (HCP) structure is presented, which has great potential for application to the ropeless elevator system. By using extensive finite element analysis (FEA), the electromagnetic properties of the proposed HCP-PMLSM, including magnetic field, back electromagnetic force (back-EMF), thrust force and cogging force are simulated and compared with the consequent pole PMLSM (CP-PMLSM) and surface-mounted pole PMLSM (SP-PMLSM). The comparison results show that the proposed HCP configuration can reduce substantial PM material and increase the air-gap magnetic field effectively. Then, the influence trend of HCP parameters such as pole thickness, pole width ratio, auxiliary PM width and magnetism angle, are studied and analyzed for evaluating the output performance in HCP-PMLSM. On this basis, Response surface method (RSM) is employed to optimize the HCP parameters with the target of maximum average thrust, minimum thrust ripple, and highest PM utilization. Furthermore, a double-sided pole shift method was proposed to significantly suppress the thrust fluctuation of HCP-PMLSM. Lastly, experimental results are provided to verify the investigation.

INDEX TERMS Consequent pole, Halbach, linear motor, pole optimization, permanent magnet motor, thrust ripple.

I. INTRODUCTION

With the emergence of high-rise and super high-rise skyscrapers, the traditional elevator driven by rotary motor through counterweight is no longer applicable. Limited by the interference of hoisting rope, a large number of single hoist way has to be used, which takes up a lot of building space, and the long hall waiting time is intolerable. Therefore, the multi-car ropeless elevator driven by linear motor is proposed to solve these problems [1]–[3]. Permanent magnet linear synchronous motor (PMLSM) has been proven to be the most attractive and potential driving source for ropeless elevators due to the advantages of high speed, high thrust density, high power density, high power factor and high reliability [4]–[6]. In order to achieve independent control of multiple cars without winding switching, the ropeless elevator scheme generally adopts the secondary PM plates of PMLSM to be laid along the entire hoist way track, and the primary winding moves with the car. While, this scheme needs a large amount of PM materials and leads to the cost increase for PMLSM. So, it is necessary and valuable work to reduce the amount of PMs and thus reduce the overall cost of this kind of motor.

In recent years, many experts have studied the new topologies and mechanisms [7]–[9], electromagnetic design [10]–[12], advanced control methods [13]–[15] and fault

The associate editor coordinating the review of this manuscript and approving it for publication was Shihong Ding.

diagnosis [16]–[18] on special electrical machines, all of which are mainly focused on improving performance and reducing costs. Consequent pole (CP) arrangement for PM motor is that one PM pole is set between two salient ferromagnetic iron poles and saves half the number of PM poles, thereby reducing motor costs. So, the CP structure is a cost-effective solution and has been studied and investigated extensively to reduce PM usage and achieve acceptable performance in PM motor [19]–[25], vernier machine [26], [27], flux-reversal machine [28], [29], and coaxial PM gear [30], [31]. PMLSM with CP poles in secondary plate has high utilization coefficient of rare earth PMs. But severe flux leakage exists between the PM and adjacent iron poles, resulting in a performance reduction [32], [33].

In order to improve the problems of the aforementioned CP motors, we propose a new HCP structure for PMLSM. In the Halbach array, radial and tangential PM segments are assembled to concentrate the magnetic field and thus strengthen the air-gap flux density [34]–[37]. The proposed HCP-PMLSM configuration combining the features of high PM utilization in the CP motor and high flux density in Halbach array. Extensive finite element analysis is performed first to reveal the characteristics of HCP-PMLSM, which are compared thereafter with those of SP-PMLSM and CP-PMLSM. The characteristics include open-circuit air gap flux density, cogging force, induced voltage, average thrust, thrust ripple, and power factor. Then, the influence trend of HCP parameters such as pole thickness, pole width ratio, auxiliary PM width and magnetism angle, are studied and analyzed, the aforesaid parameters are optimized thereafter for high average thrust, high PM utilization, and low thrust ripple. Furthermore, a double-sided pole shift method was proposed, thereby significantly suppressing the thrust ripple in HCP-PMLSM. Lastly, the validity of these analyses is confirmed by prototype experimental results.

II. PMLSM WITH DEFFERENT POLE CONFIGURATIONS

Figure 1(a) schematically shows the geometry of SP-PMLSM for ropeless propulsion, which includes primary and secondary features. Figure 1(b) and 1(c) show the geometries of the corresponding CP-PMLSM and HCP-PMLSM, respectively. In the secondary CP-PMLSM, one salient ferromagnetic iron is set between two PM poles, and the magnetic direction of all PM poles is the same. In this case, the PM volume can be saved. To concentrate the flux in CP-PMLSM, tangential magnetized PMs are inserted between radial magnetized PMs and iron poles. Consequently, the proposed HCP-PMLSM is formed. Table 1 lists the major specifications of the three models. For reasonable comparison, the primaries, airgap length, laminated length, electrical rating, and main design parameters of the three models are the same. However, the only difference is the topology of the poles. To overcome normal magnetic attraction, which is often several times the rated thrust, the structure scheme of double-sided with conjugate secondary is used. The windings of the corresponding phases of double-side primary are

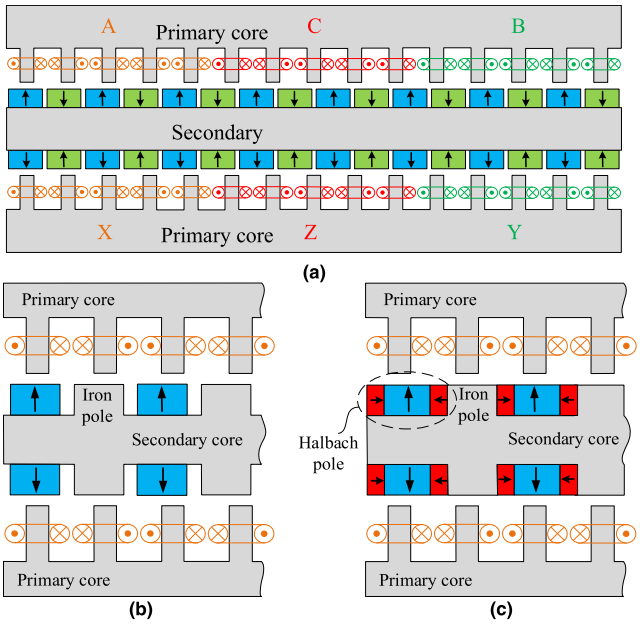

FIGURE 1. Cross section of three PMLSMs. (a)Conventional SP-PMLSM. (b)CP-PMLSM. (c)Proposed HCP-PMLSM.

TABLE 1. Main design parameters of three PMLSMs.

Parameter	SP-PMLSM	CP-PMLSM	HCP-PMLSM
Pole pitch (mm)	22.5	22.5	22.5
PM height (mm)	11	11	11
Radial magnetized PM width (mm)	20	20	20
Tangential magnetized PM width (mm)	/	/	2.5
Iron pole height (mm)	/	11	11
Iron pole width (mm)	/	20	20
Primary height (mm)	45	45	45
Secondary height (mm)	25	25	25
Tooth height (mm)	20	20	20
Air gap length (mm)	4	4	4
Laminated length (mm)	70	70	70
PM remanence at 20°C (T)	1.39	1.39	1.39
PM relative permeability	1.04	1.04	1.04

connected in series. By this structure scheme, the pressure on the linear bearing could be significantly reduced, thereby simplifying the mechanical components. The authors have revealed that SP-PMLSM of the geometry parameters have good electromagnetic performance and suitable for coupling ropeless elevator directly [38]. The typical ropeless elevator system generally adopts multiple unit motors to assemble along the lifting direction, thereby forming a continuous core. In this case, the end effect caused by the breaking of the primary has minimal effects on the overall electromagnetic performance of the motors. Therefore, the end effect is not considered in the two-dimension FEA by setting periodic boundary.

Fig. 2 compares field distributions of the three models on no-load condition. In CP-PMLSM and HCP-PMLSM, the flux generated by the PMs threads the air gap, primary core,

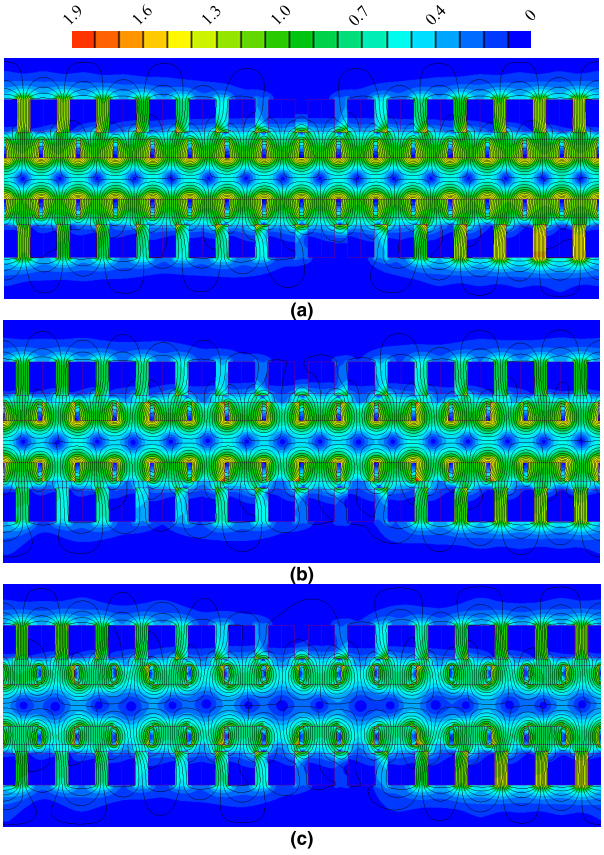

FIGURE 2. Field distribution of three models(a)conventional SP-PMLSM, (b)CP-PMLSM, (c)Proposed HCP-PMLSM.

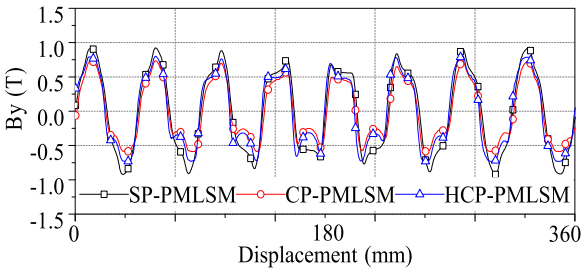

FIGURE 3. Comparison of air gap flux density.

iron pole, and secondary yoke. Consequently, a closed loop is formed, which is nearly the same as SP-PMLSM. Note that the flux density between the PM and iron poles is higher in CP-PMLSM than that in HCP-PMLSM, thereby indicating a severe flux leakage between the poles. In HCP-PMLSM, the flux leakage is suppressed effectively by inserting tangential magnetized PMs. Fig. 3 shows the normal components of the air gap flux density of the three models. Evidently, SP-PMLSM obtained the highest air-gap flux density with the most PM material, followed by HCP-PMLSM and CP-PMLSM.

Fig. 4 shows the harmonic components of the phase back-EMF in no-load condition. SP-PMLSM obtained the highest fundamental amplitude, followed by HCP-PMLSM

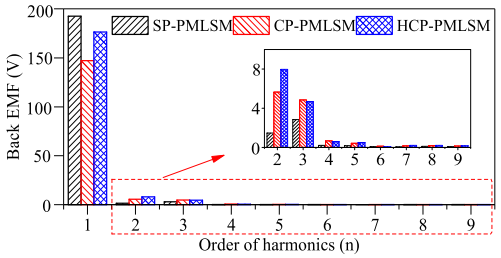

FIGURE 4. Harmonic components of voltage waveform.

and CP-PMLSM. This result is consistent with the preceding analysis. The total harmonic distortion of SP-PMLSM, CP-PMLSM, and HCP-PMLSM are 1.67%, 5.09%, and 5.26% respectively. Note that the increase in total harmonic distortion could increase thrust ripple considering that the output thrust is essentially the product of the no-load back-EMF and winding current.

Cogging force is a periodic fluctuant force that is caused by the interaction between PMs and slots, and adversely affects the smoothness of motion, particularly in low speed. The pole-slot combination is known to be the most critical factor affecting the cogging force in PM motors. The cogging force period is defined as equation (1), which indicates that an increase in the least common multiple (LCM) of slot and PM pole could diminish the cogging force magnitude and its period. That is one of the reasons that fractional slot concentrated winding PMLSM is particularly suitable for low speed direct drive. In the analysis model of SP-PMLSM, the LCM value is 240 and the period of cogging force obtained from equation (1) is 1.5 mm. In CP-PMLSM and HCP-PMLSM, the cogging force period is twice that of SP-PMLSM because one polarity of PM is missing. The predicted cogging force of the three models are compared in Fig. 5, which is consistent with the preceding analysis.

$$P_{cogging\ force} = \frac{L}{\text{LCM of } N_P \text{ and } N_S} \tag{1}$$

where $Pcogging\ force$, L, N_P, and N_S denote cogging force period, length of motor, number of PM poles, and number of slots, respectively.

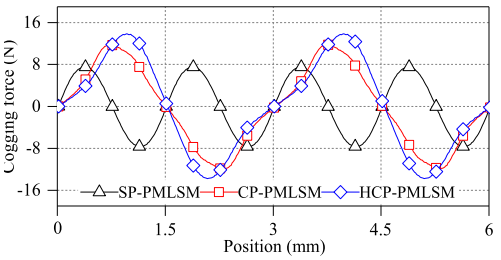

FIGURE 5. Cogging force comparison of three models.

The output thrust curves at a rated current (7 A) and speed (1.035 m/s) of the three models are compared in Fig. 6. In the analysis, the three-phase sinusoidal current is

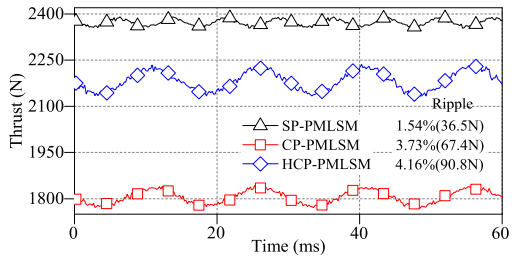

FIGURE 6. Rated thrust comparison of three models.

powered in the windings. The average thrusts of CP-PMLSM and HCP-PMLSM are approximately 75.4% (1805 N) and 91.1% (2183 N), respectively, of that of the conventional SP-PMLSM (2372 N). However, the PM volumes of CP-PMLSM and HCP-PMLSM are 50% and 62.5%, respectively, of that of SP-PMLSM. Note that the thrust fluctuations of CP-PMLSM and HCP-PMLSM are severe and may reduce the ride comfort of the elevator. Given that the peak–peak value of the thrust ripple is substantially larger than that of the cogging force, the severe thrust fluctuation can be deduced to be mainly caused by back-EMF harmonics. The thrust ripple reduction by an improved double-sided pole shift method will be discussed in the succeeding sections.

Detailed comparison of the power factor is shown in Fig. 7, which shows that the power factor of two PMLSMs with iron poles are lower than that of SP-PMLSM. However, when minimal PM material is considered, the lower power factor is acceptable when operating under a continuous condition.

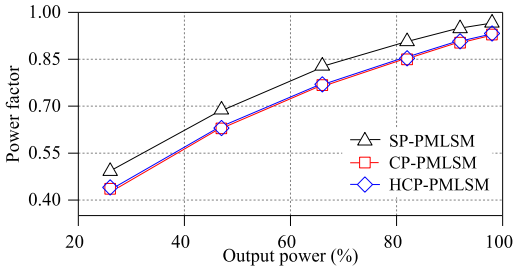

FIGURE 7. Power factor comparison of three models.

TABLE 2. Performance comparison of three machines.

Item	SP-PMLSM	CP-PMLSM	HCP-PMLSM
PM volume (cm^3)	492.8	246.4	308
Average thrust (N)	2372	1805	2183
λ_{PM} (N/cm^3)	4.81	7.33	7.09
Thrust ripple (%)	1.54	3.73	4.16

Table 2 presents the performance comparison of the three motors under rated conditions. For long secondary PMLSM in the ropeless elevator system, the amount of PM has a significant impact on manufacturing cost. Therefore, the PM utilization coefficient (λ_{PM}) is defined as the ratio of average thrust to PM volume for the motors' evaluation. The traditional SP-PMLSM obtained the highest average thrust due to the use of more PMs, whereas the lowest λ_{PM} in the three motors. CP-PMLSM has the highest λ_{PM}, whereas the lowest average thrust because of the relatively large leakage flux. The proposed HCP-PMLSM can keep a good balance on the output thrust and PM utilization. Compared with conventional SP-PMLSM, the proposed HCP-PMLSM uses 62.5%(308cm^3) of PM material and retains 92%(2183N) output thrust.

Note that the advantages of CP-PMLSM are simpler manufacturing and easier installation of secondary PM components. CP-PMLSM is particularly suitable for applications that do not require large thrust to reduce PM costs. However, when CP-PMLSM is applied in a ropeless elevator system, the output thrust is insufficient, which means that more unit motors are needed to drive the elevator car, and it will increase manufacturing costs. Considering the overall cost, HCP-PMLSM is more attractive as a drive source for ropeless elevator systems.

Moreover, an increase in polar-arc and PM dosage in SP-PMLSM and CP-PMLSM decreased the distance between poles. That is, the flux leakage between poles will become considerably serious, and the thrust will be markedly difficult to increase by increasing the PM dosage. However, the Halbach poles in the HCP arrangement are used to reduce magnetic leakage. It means that the geometry parameters of HCP continue to have the potential to be optimized for better performance, which will be investigated in the succeeding sections.

III. POLE OPTIMIZATION OF HCP-PMLSM

The main factors affecting the field distribution in a PM motor include the arrangement of PMs, length of air gap, slot in primary, and material of core, etc. In particular, the arrangement of PMs has the most influence among these factors. The constitution of poles is complex in the proposed HCP-PMLSM, and the geometry of each pole should be optimized. This section investigates the influence of the pole thickness H, PM pole ratio a_1, radial magnetized PM pole ratio a_2, and magnetism angle of auxiliary PM pole δ on the output performance of HCP-PMLSM. The four important design parameters of poles were optimized for high average thrust, high PM utilization coefficient, and low thrust ripple.

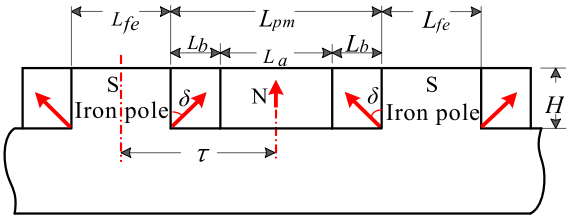

FIGURE 8. Schematic diagram of poles in HCP-PMLSM.

The geometric parameters of the HCP-PMLSM are shown in Fig. 8.

The PM poles ratio a_1 and radial magnetized PM poles ratio a_2 are defined as follows:

$$a_1 = \frac{L_{pm}}{2}\tau \tag{2}$$

$$a_2 = \frac{L_a}{L_{pm}} \tag{3}$$

where L_{pm}, τ, and L_a denote the width of the PM poles, pole pitch, and width of a radial magnetized PM pole, respectively.

A. POLES THICKNESS OPTIMIZATION

The thickness of poles is a key parameter for the performance of a PM machine. The variations of the average thrust and thrust ripple with the thickness of poles are shown in Fig. 9. The PM utilization coefficient could be observed from the slope of average thrust curve. Note that the thrust increased rapidly and eventually tended to flatten with an increase in pole thickness. The thickness of poles has a slight influence on the thrust ripple. Hence, PM could not maintain high utilization when the pole thickness is over 11 mm. Accordingly, the pole thickness is designed to be 11 mm with respect to the optimization target of high average thrust, high PM utilization, and low thrust ripple.

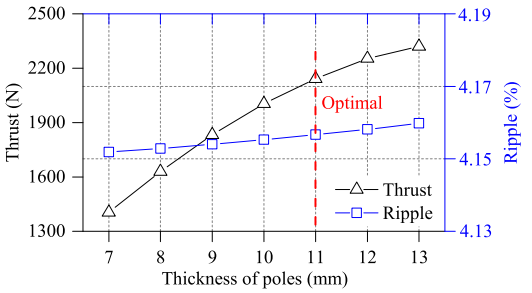

FIGURE 9. Magnet-thickness versus thrust characteristic.

B. PM POLES RATIO OPTIMIZATION

Similar to traditional SP-PMLSM, the PM-arc, which is a_1 in the preceding parameters to be optimized, is a key parameter in the proposed HCP-PMLSM. Fig. 10 shows the variations of thrust and thrust ripple with a_1 and a_2 when H and δ are equal to 11 mm and 90°, respectively. Note that the average thrust increased with an increase in a_1, and the increase rate decreased owing to the magnetic saturation when a_1 was over 0.65. Simultaneously, the average thrust increased first and decreased thereafter with an increase in a_2, thereby indicating an optimal a_2 for a certain a_1. This study designs the radial magnetized PM pole ratio a_1 to be 0.65. Accordingly, the motor simultaneously obtained relatively superior performance of the average thrust, PM utilization, and thrust ripple.

C. RADIAL MAGNETIZED POLES RATIO AND MAGNETIZATION ANGLE OPTIMIZATION

The preceding analysis indicates an optimal ratio of radial magnetized PM poles (a_2) under a certain PM pole ratio (a_1).

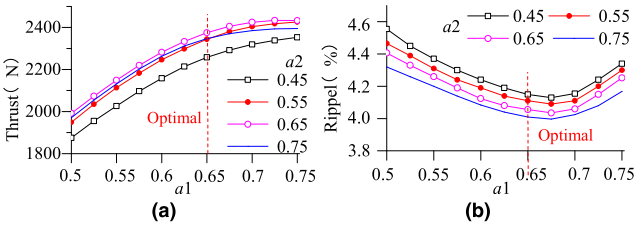

FIGURE 10. a_1 and δ versus thrust characteristic. (a) a_1 and a_2 versus average thrust. (b) a_1 and a_2 versus thrust ripple.

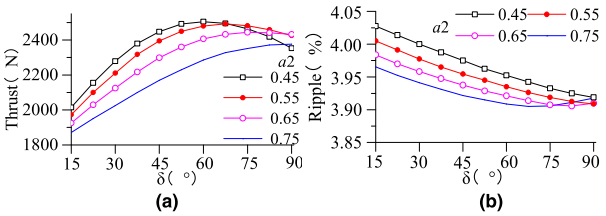

FIGURE 11. a_2 and δ versus thrust characteristic. (a) a_2 and δ versus average thrust. (b) a_2 and δ versus thrust ripple.

Moreover, the tangential magnetism for auxiliary PM poles is not necessarily the best in HCP-PMLSM. This section investigates in detail the influence of a_2 and δ on the thrust character of HCP-PMLSM when H and a_1 are equal to 11 mm and 0.65, respectively. Note that the PM volume is invariant when a_1 is determined. Thus, the variation of PM utilization coefficient is consistent with the variation of the average thrust. Figure 11 shows that when a_2 adopted 0.75, the average thrust increased with an increase in δ, and reached the maximum when δ was equal to 90°. When a_2 adopted 0.65, 0.55, and 0.45, the average thrust increased first and decreased thereafter with an increase in δ. Moreover, the maximum values were obtained when δ was equal to 75°, 67.5°, and 60°, respectively. When a_2 was 0.65 and 0.75, the thrust ripple decreased first and increased thereafter with δ, and the minimum values were obtained at 67.5° and 82.5°, respectively. When a_2 was 0.45 and 0.55, the thrust ripple decreased with an increase in δ, and the minimum value was obtained when δ is 90°. The analysis results showed that when a_2 and δ varied, the average thrust and thrust ripple varied simultaneously. Moreover, the optimal value that met the requirements of high thrust, high PM utilization, and low thrust ripple cannot be easily found from the figure.

The previous analysis indicates that the optimal values of H and a_1 are 11 mm and 0.65, respectively. However, a contradiction was observed when selecting the optimal value of a_2 and δ.

Response surface methodology is a statistical method used to solve multivariate problems. The functional relationship between objective function and optimization variables can be obtained by designing experiments reasonably. For the optimization of a_2 and δ, this study combined RSM with FEA, which has been applied invarious optimization studies with proven reliability and effectiveness [39], [40].

TABLE 3. Experimental arrays and experimental results.

Number	Variable		Coded conversion value		Average thrust (N)	Thrust ripple (%)
	a_2	δ (°)	a_2	δ (°)		
1	0.47	-18.64	0	-1.414	1667	4.07
2	0.47	45	0	0	2495	3.97
3	0.09	45	-1.414	0	2352	4.05
4	0.75	90	+1	+1	2331	3.94
5	0.47	45	0	0	2495	3.97
6	0.75	0	+1	-1	1880	3.96
7	0.47	45	0	0	2495	3.97
8	0.86	45	+1.414	0	2100	3.92
9	0.47	45	0	0	2495	3.97
10	0.20	0	-1	-1	2015	4.09
11	0.47	45	0	0	2495	3.97
12	0.47	108.64	0	1.414	2041	3.92
13	0.20	90	-1	+1	1775	3.94

By using RSM, the relationship between the objective function and the two variables could be represented by the following quadratic polynomial [41]:

$$y = a_0 + \sum_{i=1}^{k} a_i x_i + \sum_{i=1}^{k} a_{ii} x_i^2 + \sum_{i<j} \sum a_{ij} x_i x_j + \varepsilon \quad (4)$$

where y denotes the response objective function, a denotes the undetermined coefficient, ε denotes the fitting error, and x_i and x_j denote the optimization variables

This study selected a_2 and δ as the optimization variables. Average thrust and thrust ripple were chosen as the objective function. The corresponding response surfaces can be presented as follows:

$$\begin{cases} F_{avg} & = f(a_2, \delta) \\ K_r & = f(a_2, \delta) \end{cases} \quad (5)$$

An appropriate mathematical model is necessary. To establish response surface models with high coincidence coefficient. Central composite design was adopted to estimate the response models appropriately. The high and low levels of independent variables were coded as +1.414, +1, 0, −1, and −1.414, respectively. Table 3 lists the corresponding arrays and calculated results. Statistical evaluation yielded the corresponding responses, which is expressed in (6). The response models are well built because the values of R^2, which is the coincidence coefficient, are 0.9179 and 0.9554.

$$\begin{cases} F_{avg} = 1925.58262 + 1215.61157 \times a_2 \\ +10.11062 \times \delta + 13.9596 \times a_2 \times \delta \\ -1909.91736 \times a_2^2 - 0.16318 \times \delta^2 \\ \\ K_r = 4.1523 - 0.26175 \times a_2 - \delta \times 2.33437e \\ \times 10^{-3} + a_2 \times \delta \times 2.66667 \times 10^{-3} \end{cases} \quad (6)$$

Figure 12 (a) and (b) show the 3D curved surface projection of the established average thrust and thrust ripple response surfaces, respectively. Given that the volume of PM is a fixed value when a_1 is determined, the two responses could be considered to reflect the variation of the average thrust, PM utilization, and thrust ripple with different combinations of a_2 and δ. Note that the points meet the maximum thrust and minimum thrust fluctuations, which are distributed in the different areas of the two graphs. That is, no solution simultaneously satisfies the three optimization targets. Therefore, optimization becomes a problem of choosing a reasonable compromise among the three optimization targets.

The point of maximum thrust under the combination of a_2 and δ is eventually selected as the optimal solution. In this trade-off case, the optimal target of the maximum PM utilization coefficient can be satisfied and the ripple was relatively compromised. The contour map formed by the response surfaces shows that the optimal combination of a_2 and δ is $(a_2, \delta) = (0.51, 52.84°)$ can be obtained. The corresponding average thrust, PM utilization coefficient, and thrust ripple are 2503 N, 6.94 N/cm^3, and 3.97%, respectively.

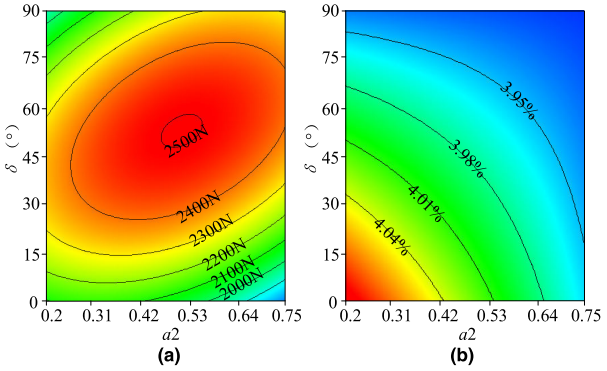

FIGURE 12. Curved surface projection of response surfaces. (a) Response surface of average thrust. (b) Response surface of thrust ripple.

Fig. 12(a) shows that in HCP-PMLSM, PMs were not completely utilized when the auxiliary PM poles were with tangential magnetism. To further investigate this difference, two finite element models based on $(a_2, \delta) = (0.51, 90°)$ and $(a_2, \delta) = (0.51, 52.84°)$ were established. Fig. 13 shows the field distributions over a range of pole pairs for two models in a no-load condition. The magnetization directions of PMs are indicated by arrows, and the flux paths generated by PMs

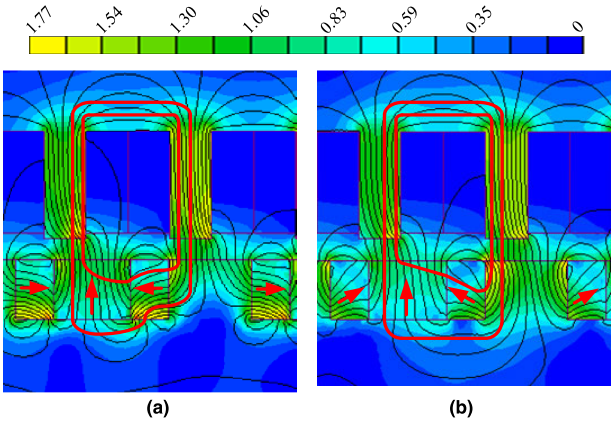

FIGURE 13. Flux distribution of HCP-PMLSM with different value of δ when no-load. (a) $(a_2, \delta) = (0.51, 90°)$. (b) $(a_2, \delta) = (0.51, 52.84°)$.

TABLE 4. Comparisons between RSM and FEA results.

Item	Average thrust (N)		Thrust ripple (%)	
	RSM	FEA	RSM	FEA
Model1(0.51,90°)	2278	2257	3.93	3.91
Model2(0.51,52.84°)	2504	2499	3.97	3.96

are circuited by red lines. Note that the difference lies in the outer circle, which is generated using radial magnetized PM. When the auxiliary PM is tangentially magnetized, the flux is generated by the radial magnetized PM passing through auxiliary PMs to form a closed loop. However, when the magnetism of auxiliary PMs is adjusted to an optimal angle, this part of the flux directly forms a closed loop through the iron pole. This outcome shortened the magnetic circuit, and additional magnetic flux was obtained. In HCP-PMLSM, the tangential magnetization of the auxiliary PMs is not the ideal to raise air gap flux density, which is different from the conventional Halbach array. Moreover, Figure 11(a) and 12(a) indicate that the optimal magnetism angle varies with variations in a_1 and a_2. The thrust characteristics of the two models at rated conditions are calculated and compared with the values predicted by RSM. Table 4 shows that the average thrust and thrust ripple obtained by FEA and RSM showed good agreement, thereby verifying the validity of the response surface optimization method. HCP-PMLSM could achieve 5.3% higher output capacity at a rated state when compared with SP-PMLSM with 27.6% less PM material.

IV. THRUST RIPPLE SUPPRESSING BY DOUBLE-SIDED ASYMMETRY ARRANGEMENT

A. FINITE ELEMENT MODEL AND FIELD COMPUTATION

For PMLSMs in the ropeless elevator system, thrust ripple deteriorates the motion smoothness and ride comfort. Thus, the suppression of thrust ripple is an important aspect for the successful application of the proposed HCP-PMLSM. This study proposes a double-sided pole shift method to overcome the asymmetric air gap flux above the PM and iron poles in HCP-PMLSM, thereby suppressing the thrust

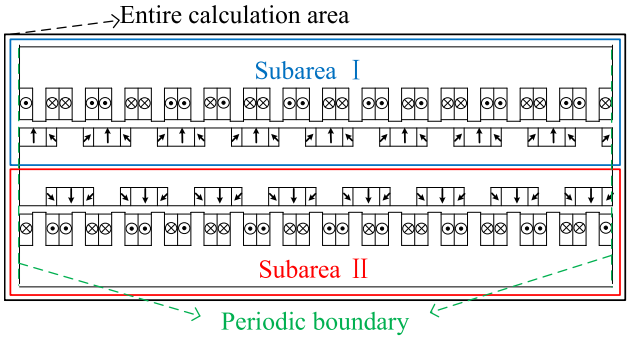

FIGURE 14. Sub-areas in finite element model in proposed double-sided asymmetry arrangement.

ripple. As shown in Fig. 14, the poles of the double sides are staggered by a pole pitch distance, thus the double-sided asymmetry arrangement is formed. Given that the spatial electrical angle difference of primaries in the two sides are 180°, the windings belonging to the same phase in the two primaries are wound reversely, as shown by the windings return (X) and go (•).

In general, the calculation area in a double-sided PMLSM finite element model covered the double sides. This study introduces two sub-areas for conventional double-sided arrangement and the proposed double-sided asymmetry arrangement to completely investigate the effects of thrust ripple suppression. As shown in Fig. 14, each sub-area contains a single-sided motor. The two sub-areas are called Sub-area I and II. To show feasibility, detailed electromagnetic performances were compared between conventional symmetry topology and proposed asymmetry topology, including the cogging force, self-inductance, no-load back-EMF, and thrust character on rated state.

B. RIPPLE SUPPRESSION PRINCIPLE OF PROPOSED SCHEME

The suppression of thrust ripple can be best explained by the calculated results of the two sub-areas. The phases of Sub-area I and II are mutually 180 electrical degrees apart by placing each other one pole-pitch apart. Given this arrangement, thrust ripples rooted in magnetic unbalance could be offset.

Figs. 15 to 19 show that the calculated results of Sub-area I and II at no-load and rated state could illustrate the principal of ripple suppression. Fig. 15 shows the cogging force of HCP-PMLSM in the conventional and proposed asymmetry topology. Each sub-area suffered severe ripples. Nevertheless, the resultant cogging force of the double-sided asymmetry topology was significantly reduced because the half-period difference of the pulsating ripple in two sides. Compared with conventional topology, the proposed asymmetry topology reduced the peak–peak value of the cogging force from 17.2 N to 4.7 N.

The self-inductance characteristic is an important parameter of the PM machine because a stable self-inductance is

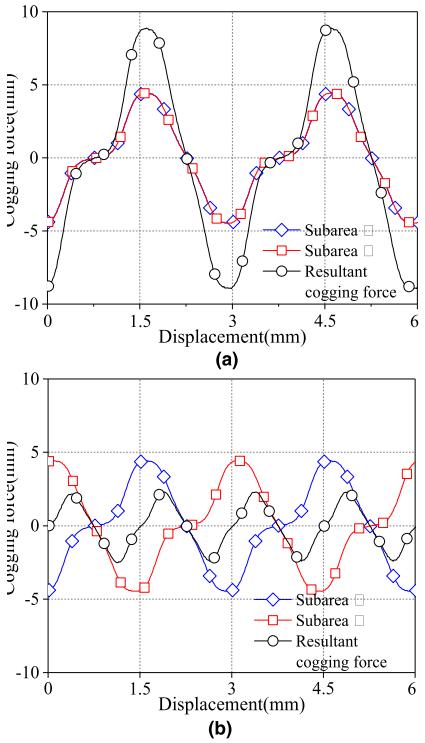

FIGURE 15. Comparison of cogging force. (a) Conventional topology. (b) Asymmetry topology.

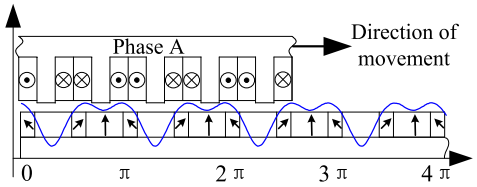

FIGURE 16. Self-inductance versus different primary position.

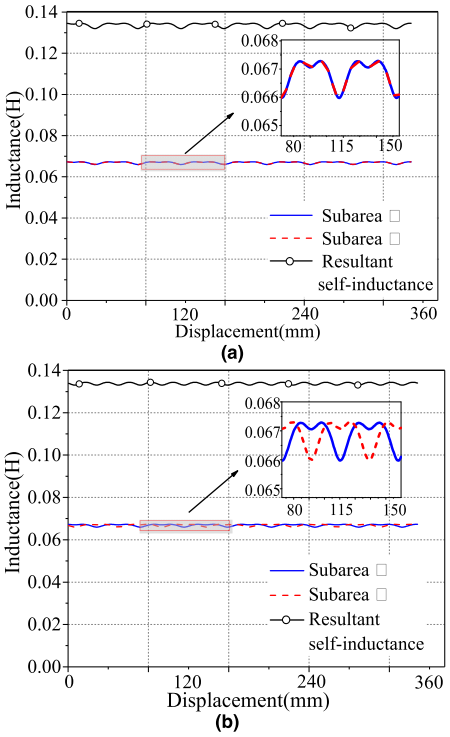

FIGURE 17. Comparison of self-inductance. (a) Conventional topology. (b) Asymmetry topology.

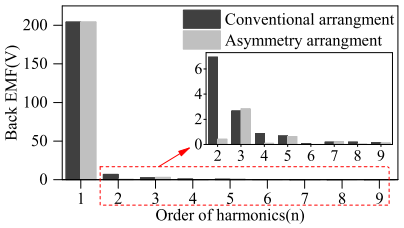

FIGURE 18. Harmonic components of voltage waveform.

necessary for the smoothness of output thrust. Figure 16 shows the variation of self-inductance with displacement in HCP-PMLSM solved using the finite element method. The value of self-inductance was minimal when the primary windings moved to the position where the interlink flux with PM was the largest. Meanwhile, self-inductance was at a maximum when the primary coils moved to the position where the interlink flux with PM was least. The period of self-inductance fluctuation was twice the pole pitch, as one polarity of PM was missing. Figure 17 shows the comparison of the consultant self-inductance in two kinds of double-sided topologies. The resultant ripple of self-inductance in the double-sided asymmetry topology was significantly reduced because of the half-period difference of pulsating ripple in two sides. The average value of self-inductance in two topologies was the same, but the ripple declined 49% by the asymmetry arrangement, which was reduced from 1.97% to 1.00%.

Figure 18 compares the harmonic content of the back-EMF under two types of arrangements at no-load state. The arrangements had nearly equivalent fundamental and odd-order harmonics, while even-order harmonics were extremely low in the proposed asymmetry topology. The even order harmonics in the back-EMF were eliminated as the antiphase in the two sub-areas, which can be expounded as follows.

If the winding resistance and structural asymmetry could be disregarded, then the induced voltage of each section can be expressed as the superimposition of even and odd order harmonics. Thus, the induced voltage of Sub-areas I and II can be expressed as follows:

$$u_1 = \sum_{i}^{i=1,3,5\ldots} u_{im} sin(iwt + \theta_i) + \sum_{j}^{j=2,4,6\ldots} u_{jm} sin(jwt + \theta_j) \tag{7}$$

$$u_2 = \sum_{i}^{i=1,3,5\ldots} u_{im} sin(i(wt + \pi) + \theta_i + \pi) + \sum_{j}^{j=2,4,6\ldots} u_{jm} sin(j(wt + \pi) + \theta_j + \pi) \tag{8}$$

where u_{im} and u_{jm} denote the amplitudes of the i-th and j-th harmonics, θ_i and θ_j denote the initial position of primary.

The resultant windings voltage of two sub-areas can be calculated by adding (7) and (8):

$$\begin{aligned} u &= u_1 + u_2 \\ &= \sum_{i=1,3,5...}^{i} u_{im}[sin(iwt + \theta_i) + sin(iwt + \theta_i + \varphi_1)] \\ &= \sum_{j=2,4,6...}^{j} u_{jm}[sin(jwt + \theta_j) + sin(jwt + \theta_j + \varphi_2)] \quad (9) \end{aligned}$$

$$\begin{cases} \varphi_1 = (i+1)\pi \\ \varphi_2 = (j+1)\pi \end{cases} \quad (10)$$

in the double-sided asymmetry arrangement, the even-order harmonics of Subarea I are canceled by those of Subarea I because $(j + 1)$ is constantly odd. However, the fundamental and odd-order harmonics are added directly because $(i + 1)$ is consistently even.

Fig. 19 compares the rated thrust of the two models for HCP-PMLSM. The average thrust is nearly not reduced, but the thrust fluctuation can be effectively suppressed by the proposed asymmetry topology.

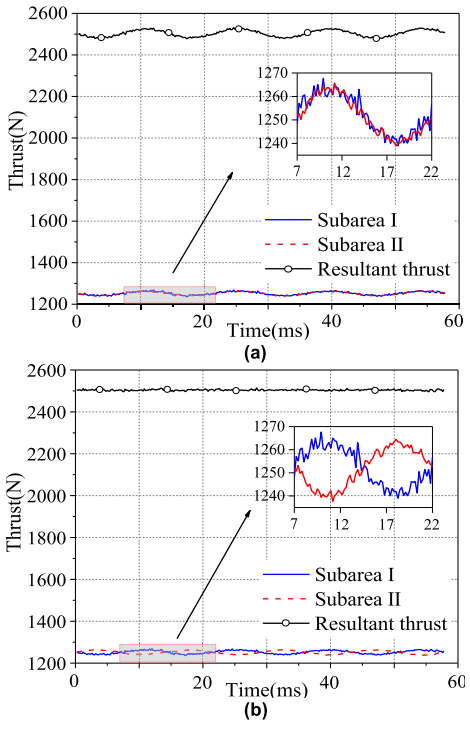

FIGURE 19. Comparison of rated thrust. (a) Conventional symmetry topology. (b) Asymmetry topology.

Table 5 shows the performance comparison between the optimized HCP-PMLSM and traditional SP-PMLSM under the rated condition. The proposed HCP-PMLSM with double-sided asymmetry arrangement had high average thrust and lower thrust ripple, and reduced the usage of the PM material by 27.6% compared with that of SP-PMLSM. Moreover, the PM material utilization coefficient increased by 44.2%.

TABLE 5. Performance comparison between SP-PMLSM and optimized HCP-PMLSM.

Item	SP-PMLSM	Optimized HCP-PMLSM
PM volume (cm^3)	492.8	360.36
Average thrust (N)	2372	2499
λ_{PM} (N/cm^3)	4.81	6.94
Thrust ripple (%)	1.54	0.87

V. EXPERIMENTATIONS

The HCP-PMLSM experimental prototype is manufactured, and it consists of two parts: the secondary PMs plate and the primary iron-core module, as shown in Fig.20(a) and (b). The experimental bench includes the proposed HCP-PMLSM prototype under test and the SP-PMLSM motor for driving, and the two are hard-connected through a force sensor, as shown in Fig.20(c). The SP-PMLSM motor is used as a servo traction motor to push the HCP-PMLSM to move at a constant speed, so as to test the back EMF and thrust of HCP-PMLSM.

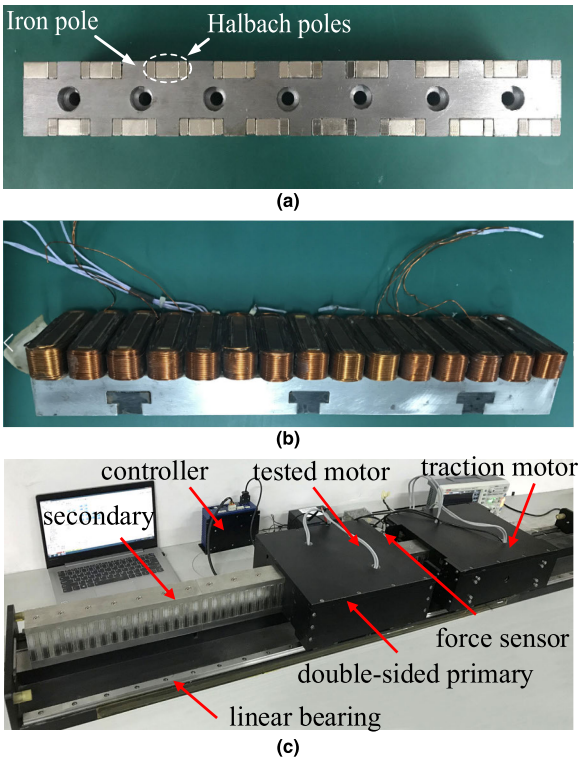

FIGURE 20. Prototype(a) Secondary of HCP-PMLSM, (b) Primary of HCP-PMLSM, (c) Experiment bench.

The primary winding of the HCP-PMLSM under test is dragged by a servo traction motor, the back-EMF at no-load is measured, and the detent force is obtained by the force sensor. Figure 21 (a) shows the comparison curve of the

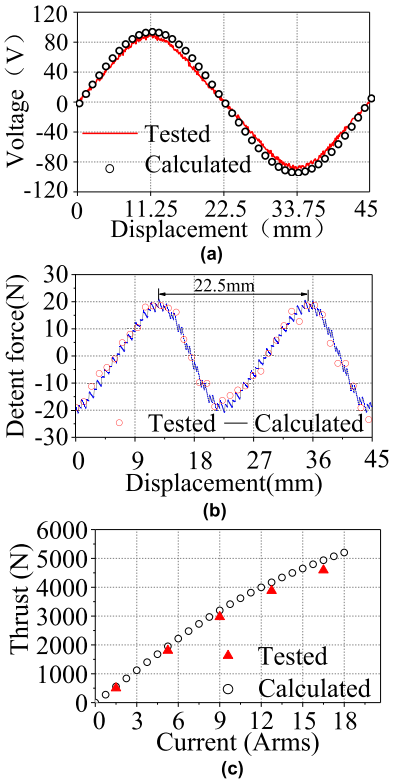

FIGURE 21. Comparison of FEA and measured results (a) Open-circuit back-EMF, (b) Detent force, (c) Static thrust versus current.

line-to-line back-EMFs based on the finite element and the experimental test value at 0.2 m/s. The finite element calculated waveform is basically consistent with the measured one. The slight deviation may be due to the neglect of the lateral edge effect in the 2D finite element analysis. The detent force, which is consisted of end force and cogging force, is measured and shown in Fig. 21(b). The finite element calculating value and tested detent force agree with each other basically, it fluctuates with a single cycle as the mover travels one pole pitch distance. The ripple waveform evidence that the cogging force is reduced greatly and the detent force is mainly caused by end force.

When the windings are powered by a DC current, the static thrust loads on the mover, which varies as the position as the primary is dragged. The thrust was at a maximum when the current approximated the quadrature-axis current, whereas the minimum thrust corresponded to the direct-axis current. Fig. 21(c) shows the maximum static thrust variation when the windings were powered by different currents. The tested thrust broadly corresponded with the finite element calculating value, while the amplitudes were below the calculated results with 5.6% maximum deviation. This difference may have resulted from the assembly tolerance, impact of friction, or transverse end effect.

VI. CONCLUSION

This study proposed a novel PMLSM with Halbach consequent poles. Extensive FEA was performed to reveal the proposed motor's performance characteristics, including air gap flux density, back-EMF, average thrust, cogging force, thrust ripple and so on. The analysis results show that the proposed HCP-PMLSM effectively reduces the use of PMs and maintains a considerable output capacity, so it has good cost-effective performance.

RSM combined with FEA was adopted to optimize the parameters of the poles in HCP-PMLSM for superior output capability and quality. After the optimization design process, the thrust output increased by 5.35%, and PM usage was reduced by 27.6% compared with that of traditional SP-PMLSM.

To suppress the thrust ripple in HCP-PMLSM, the topology of double-sided shift one pole pitch distance is proposed. This topology was extensively verified by FEA and experiments, and could offset magnetic unbalance, thereby suppressing the thrust ripple.

The proposed HCP-PMLSM can be successfully implemented in ropeless elevators and other cost-sensitive applications. In the future, we will focus on the high-performance control model and algorithm of proposed motor based on their characteristics analysis in this paper.

REFERENCES

[1] H. Fan, K. T. Chau, C. Liu, L. Cao, and T. W. Ching, "Quantitative comparison of novel dual-PM linear motors for ropeless elevator system," *IEEE Trans. Magn.*, vol. 54, no. 11, Nov. 2018, Art. no. 8106506.

[2] S.-G. Lee, S.-A. Kim, S. Saha, Y.-W. Zhu, and Y.-H. Cho, "Optimal structure design for minimizing detent force of PMLSM for a ropeless elevator," *IEEE Trans. Magn.*, vol. 50, no. 1, Jan. 2014, Art. no. 4001104.

[3] X. Wang, Z. Zhang, X. Xu, and Y. Cui, "Influence of using conditions on the performance of PM linear synchronous motor for ropeless elevator," in *Proc. Int. Conf. Electr. Mach. Syst.*, Beijing, China, Aug. 2011, pp. 1–5.

[4] L. Yan, "Development and application of the maglev transportation system," *IEEE Trans. Appl. Supercond.*, vol. 18, no. 2, pp. 92–99, Jun. 2008.

[5] L. Chunyan and K. Baoquan, "Research on electromagnetic force of large thrust force PMLSM used in space electromagnetic launcher," *IEEE Trans. Plasma Sci.*, vol. 41, no. 5, pp. 1209–1213, May 2013.

[6] Z. Zhang, H. Zhou, J.-A. Duan, and B. Kou, "Research on permanent magnet linear synchronous motors with ring windings for electromagnetic launch system," *IEEE Trans. Plasma Sci.*, vol. 45, no. 7, pp. 1161–1167, Jul. 2017.

[7] L. Xie, J. Si, Y. Hu, and Z. Wang, "Overview of 2-Degree-of-Freedom rotary-linear motors focusing on coupling effect," *IEEE Trans. Magn.*, vol. 55, no. 4, Apr. 2019, Art. no. 8200611.

[8] M. He, W. Xu, J. Zhu, L. Ning, G. Du, and C. Ye, "A novel hybrid excited doubly salient machine with asymmetric stator poles," *IEEE Trans. Ind. Appl.*, vol. 55, no. 5, pp. 4723–4732, Sep. 2019.

[9] K. Watanabe, T. Suga, and S. Kitabatake, "Topology optimization based on the ON/OFF method for synchronous motor," *IEEE Trans. Magn.*, vol. 54, no. 3, Mar. 2018, Art. no. 7201104.

[10] G. Du, W. Xu, J. Zhu, and N. Huang, "Effects of design parameters on the multiphysics performance of high-speed permanent magnet machines," *IEEE Trans. Ind. Electron.*, vol. 67, no. 5, pp. 3472–3483, May 2020.

[11] C. Ye, X. Liang, F. Xiong, J. Yang, W. Xu, and Y. Liu, "Design of an axial-flux PM-assisted claw-pole generator based on an equivalent magnetic circuit model," *IEEE Trans. Energy Convers.*, vol. 33, no. 4, pp. 2040–2049, Dec. 2018.

[12] Y. Guo, J. Si, C. Gao, H. Feng, and C. Gan, "Improved fuzzy-based taguchi method for multi-objective optimization of direct-drive permanent magnet synchronous motors," *IEEE Trans. Magn.*, vol. 55, no. 6, Jun. 2019, Art. no. 8102204.

[13] W. Xu, J. Zou, Y. Liu, and J. Zhu, "Weighting factorless model predictive thrust control for linear induction machine," *IEEE Trans. Power Electron.*, vol. 34, no. 10, pp. 9916–9928, Oct. 2019.

[14] K. Shi, W. Song, H. Ge, P. Xu, Y. Yang, and F. Blaabjerg, "Transient analysis of microgrids with parallel synchronous generators and virtual synchronous generators," *IEEE Trans. Energy Convers.*, vol. 35, no. 1, pp. 95–105, Mar. 2020.
[15] K. Shi, H. Ye, P. Xu, D. Zhao, and L. Jiao, "Low voltage ride through control strategy of virtual synchronous generator based on the analysis of excitation state," *IET Gener., Transmiss. Distrib.*, vol. 12, no. 9, pp. 2165–2172, May 2018.
[16] C. Gao, K. Lv, J. Si, P. Su, and C. Gan, "A physical faulty model based on coil sub-element for direct-drive permanent magnet synchronous motor with stator winding short-circuit faults," *IEEE Access*, vol. 7, pp. 151307–151319, 2019.
[17] Y. Wu, B. Jiang, and N. Lu, "A descriptor system approach for estimation of incipient faults with application to high-speed railway traction devices," *IEEE Trans. Syst., Man, Cybern. Syst.*, vol. 49, no. 10, pp. 2108–2118, Oct. 2019.
[18] Y. Wu, B. Jiang, and Y. Wang, "Incipient winding fault detection and diagnosis for squirrel-cage induction motors equipped on CRH trains," *ISA Trans.*, to be published, doi: 10.1016/j.isatra.2019.09.020.
[19] S.-U. Chung, H.-J. Lee, B.-C. Woo, J.-W. Kim, J.-Y. Lee, S.-R. Moon, and S.-M. Hwang, "A feasibility study on a new doubly salient permanent magnet linear synchronous machine," *IEEE Trans. Magn.*, vol. 46, no. 6, pp. 1572–1575, Jun. 2010.
[20] S.-U. Chung, J.-W. Kim, B.-C. Woo, D.-K. Hong, J.-Y. Lee, and D.-H. Koo, "A novel design of modular three-phase permanent magnet Vernier machine with consequent pole rotor," *IEEE Trans. Magn.*, vol. 47, no. 10, pp. 4215–4218, Oct. 2011.
[21] S.-U. Chung, J.-M. Kim, D.-H. Koo, B.-C. Woo, D.-K. Hong, and J.-Y. Lee, "Fractional slot concentrated winding permanent magnet synchronous machine with consequent pole rotor for low speed direct drive," *IEEE Trans. Magn.*, vol. 48, no. 11, pp. 2965–2968, Nov. 2012.
[22] S.-U. Chung, J.-W. Kim, Y.-D. Chun, B.-C. Woo, and D.-K. Hong, "Fractional slot concentrated winding PMSM with consequent pole rotor for a low-speed direct drive: Reduction of rare Earth permanent magnet," *IEEE Trans. Energy Convers.*, vol. 30, no. 1, pp. 103–109, Mar. 2015.
[23] S.-U. Chung, S.-H. Moon, D.-J. Kim, and J.-M. Kim, "Development of a 20-Pole–24-Slot SPMSM with consequent pole rotor for in-wheel direct drive," *IEEE Trans. Ind. Electron.*, vol. 63, no. 1, pp. 302–309, Jan. 2016.
[24] S. Teymoori, A. Rahideh, H. Moayed-Jahromi, and M. Mardaneh, "2-D analytical magnetic field prediction for consequent-pole permanent magnet synchronous machines," *IEEE Trans. Magn.*, vol. 52, no. 6, Jun. 2016, Art. no. 8202114.
[25] X. Huang, J. Liang, B. Zhou, C. Zhang, L. Li, and D. Gerada, "Suppressing the thrust ripple of the consequent-pole permanent magnet linear synchronous motor by two-step design," *IEEE Access*, vol. 6, pp. 32935–32944, 2018.
[26] H. Wang, S. Fang, H. Yang, H. Lin, D. Wang, Y. Li, and C. Jiu, "A novel consequent-pole hybrid excited Vernier machine," *IEEE Trans. Magn.*, vol. 53, no. 11, pp. 1–4, Nov. 2017.
[27] D. Li, R. Qu, J. Li, and W. Xu, "Consequent pole toroidal winding outer rotor Vernier permanent magnet machines," *IEEE Trans. Ind. Appl.*, vol. 51, no. 6, pp. 4470–4481, Dec. 2015.
[28] S.-U. Chung, H.-J. Lee, and S.-M. Hwang, "A novel design of linear synchronous motor using FRM topology," *IEEE Trans. Magn.*, vol. 44, no. 6, pp. 1514–1517, Jun. 2008.
[29] Y. Gao, R. Qu, D. Li, J. Li, and G. Zhou, "Consequent-pole flux-reversal permanent-magnet machine for electric vehicle propulsion," *IEEE Trans. Appl. Supercond.*, vol. 26, no. 4, Jun. 2016, Art. no. 5200105.
[30] M. Chen, K. T. Chau, W. Li, and C. Liu, "Cost-effectiveness comparison of coaxial magnetic gears with different magnet materials," *IEEE Trans. Magn.*, vol. 50, no. 2, pp. 821–824, Feb. 2014.
[31] J.-X. Shen, H.-Y. Li, H. Hao, and M.-J. Jin, "A coaxial magnetic gear with consequent-pole rotors," *IEEE Trans. Energy Convers.*, vol. 32, no. 1, pp. 267–275, Mar. 2017.
[32] J. Li and K. Wang, "Analytical determination of optimal PM-arc ratio of consequent-pole permanent magnet machines," *IEEE/ASME Trans. Mechatronics*, vol. 23, no. 5, pp. 2168–2177, Oct. 2018.
[33] J. Li, K. Wang, and F. Li, "Analytical prediction of optimal split ratio of consequent-pole permanent magnet machines," *IET Electric Power Appl.*, vol. 12, no. 3, pp. 365–372, Mar. 2018.
[34] Z. Q. Zhu and D. Howe, "Halbach permanent magnet machines and applications: A review," *IEE Proc. Electr. Power Appl.*, vol. 148, no. 4, p. 299, Jul. 2001.
[35] H. Wang, J. Li, R. Qu, J. Lai, H. Huang, and H. Liu, "Study on high efficiency permanent magnet linear synchronous motor for maglev," *IEEE Trans. Appl. Supercond.*, vol. 28, no. 3, pp. 1–5, Apr. 2018.
[36] Y. Chen, W. Zhang, J. Z. Bird, S. Paul, and K. Zhang, "A 3-D analytic-based model of a null-flux Halbach array electrodynamic suspension device," *IEEE Trans. Magn.*, vol. 51, no. 11, pp. 1–5, Nov. 2015.
[37] Z. Zhang, L. Shi, K. Wang, and Y. Li, "Characteristics investigation of single-sided ironless PMLSM based on Halbach array for medium-speed maglev train," *CES Trans. Electr. Mach. Syst.*, vol. 1, no. 4, pp. 275–382, Dec. 2017.
[38] X. Zhang, X. Wang, X. Xu, and H. Feng, "Slot-pole combinations research of permanent-magnet linear synchronous motor with concentrated windings," in *Proc. 17th Int. Conf. Electr. Mach. Syst. (ICEMS)*, Hangzhou, China, Oct. 2014, pp. 1322–1325.
[39] J. Zhu, S. Li, D. Song, Q. Han, J. Wang, and G. Li, "Multi-objective optimisation design of air-cored axial flux PM generator," *IET Electric Power Appl.*, vol. 12, no. 9, pp. 1390–1395, Nov. 2018.
[40] J.-K. Lee, D.-H. Jung, J. Lim, K.-D. Lee, and J. Lee, "A study on the synchronous reluctance motor design for high torque by using RSM," *IEEE Trans. Magn.*, vol. 54, no. 3, Mar. 2018, Art. no. 8103005.
[41] K. Abbaszadeh, F. Rezaee Alam, and M. Teshnehlab, "Slot opening optimization of surface mounted permanent magnet motor for cogging torque reduction," *Energy Convers. Manage.*, vol. 55, pp. 108–115, Mar. 2012.

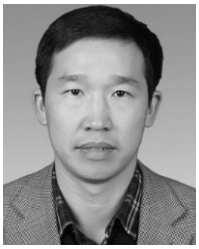

XIAOZHUO XU (Member, IEEE) was born in China, in 1981. He received the Ph.D. degree from Henan Polytechnic University, in 2016. He joined the School of Electrical Engineering and Automation, Henan Polytechnic University, in 2006, as an Associate Professor. His research interests include electrical machine design, intelligent control, and fault diagnosis.

ZHEN SUN received the B.Sc. degree in electrical engineering and automation from Henan Polytechnic University, Henan, China, in 2017, where he is currently pursuing the M.Sc. degree. His research interests include modeling, design, and control of permanent magnet linear motors.

BAOYU DU was born in Nanyang, China, in 1980. She received the B.Sc. and M.Sc. degrees from Henan Polytechnic University, in 2002 and 2006, respectively. She is currently pursuing the Ph.D. degree with Shanghai University. She joined the School of Mechanical and Power Engineering, Henan Polytechnic University, in 2006. Her research interests include electrical machine analysis and mechatronic design.

LIWANG AI (Member, IEEE) was born in Xinxiang, China, in 1989. He received the Ph.D. degree from the Institute of Electrical Engineering, Chinese Academy of Sciences, in 2019. Since July 2019, he has been with the School of Electrical Engineering and Automation, Henan Polytechnic University, where he is currently a Lecturer. His main research interests include applied superconductivity, and design and analysis of special electrical machine.